ADVANCED MATERIALS
www.advmat.de

Fine Multi-Phase Alignments in 2D Perovskite Solar Cells with Efficiency over 17% via Slow Post-Annealing

Guangbao Wu, Xing Li, Jiyu Zhou, Jianqi Zhang, Xuning Zhang, Xuanye Leng, Peijun Wang, Ming Chen, Dongyang Zhang, Kui Zhao, Shengzhong (Frank) Liu, Huiqiong Zhou,* and Yuan Zhang**

Layered Ruddlesden–Popper (RP) phase (2D) halide perovskites have attracted tremendous attention due to the wide tunability on their optoelectronic properties and excellent robustness in photovoltaic devices. However, charge extraction/transport and ultimate power conversion efficiency (PCE) in 2D perovskite solar cells (PSCs) are still limited by the non-eliminable quantum well effect. Here, a slow post-annealing (SPA) process is proposed for $BA_2MA_3Pb_4I_{13}$ ($n = 4$) 2D PSCs by which a champion PCE of 17.26% is achieved with simultaneously enhanced open-circuit voltage, short-circuit current, and fill factor. Investigation with optical spectroscopy coupled with structural analyses indicates that enhanced crystal orientation and favorable alignment on the multiple perovskite phases (from the 2D phase near bottom to quasi-3D phase near top regions) is obtained with SPA treatment, which promotes carrier transport/extraction and suppresses Shockley–Read–Hall charge recombination in the solar cell. As far as it is known, the reported PCE is so far the highest efficiency in RP phase 2D PSCs based on butylamine (BA) spacers ($n = 4$). The SPA-processed devices exhibit a satisfactory stability with <4.5% degradation after 2000 h under N_2 environment without encapsulation. The demonstrated process strategy offers a promising route to push forward the performance in 2D PSCs toward realistic photovoltaic applications.

Perovskite solar cell (PSCs) based on 3D hybrid organic–inorganic perovskite thin films have received impressive progress in the power conversion efficiencies (PCE) in the last couple of years.[1–7] However, 3D PSCs generally suffer from the issues of instability, a primary obstacle for realistic applications based on this photovoltaic technology. In comparison to 3D perovskites, emerging Ruddlesden–Popper (RP) phase 2D halide perovskites have shown excellent materials robustness under ambient environment.[8–11] The composition of this family of materials is described by the formula $(RNH_3)_2A_{n-1}M_nX_{3n+1}$ (n = 1, 2, 3, 4...) with RNH_3 being the large aliphatic or aromatic alkylammonium spacer cation, A being the monovalent organic cation, M being the divalent metal cation, and X being the halide anion.[8] Among the variety of organic spacer cations,[12–18] butylamine (BA)-based 2D perovskite PSCs have received the most attention, owing to the suitable ionic radius and excellent flexibility of BA molecule.[8,10,11,19] Based on $BA_2MA_3Pb_4I_{13}$ (n = 4) layered perovskites, Mohite et al. reported a hot-casting method to increase the vertical alignment of BA spacers, achieving a PCE of 12.52% with minimized hysteresis and good stability.[10] Attempts with solvent engineering were reported for the processing of 2D perovskite films by which enhanced charge transport properties with improved morphology were achieved.[20–22] In addition, through modification on the 2D organic cations with larger size PEA, it was found that the interplane coupling in 2D perovskites could be enhanced, leading to modified out-of-plane (OOP) carrier transport relevant to the operation of perovskite solar cells.[4,23] Through cesium based elemental doping, Liu and co-workers recently reported $BA_2MA_3Pb_4I_{13}$ PSCs with a PCE exceeding 13%.[8] In our previous study, we proposed a p–i–n structure with all organic charge transporting layers for $BA_2MA_3Pb_4I_{13}$ solar cells with a PCE of 14.3%.[19] Interestingly the efficiency exhibited a negative temperature dependence, reaching 15% at 210 K.

Although enhanced charge transport/extraction and eventual PCEs in $BA_2MA_3Pb_4I_{13}$ based PSCs have been benefitted from the efforts on modifying the vertical alignment of BA spacer cations, the detrimental effect of quantum wells is

G. Wu, Dr. X. Li, J. Zhou, X. Zhang, D. Zhang, Prof. Y. Zhang
School of Chemistry
Beijing Advanced Innovation Center for Biomedical Engineering
Beihang University
Beijing 100191, China
E-mail: yuanzhang@buaa.edu.cn
Dr. J. Zhang, X. Leng, Prof. H. Zhou
CAS Key Laboratory of Nanosystem and Hierarchical Fabrication
CAS Center for Excellence in Nanoscience
National Center for Nanoscience and Technology
Beijing 100190, China
E-mail: zhouhq@nanoctr.cn
P. Wang, M. Chen, Prof. K. Zhao, Prof. S. Liu
Key Laboratory of Applied Surface and Colloid Chemistry
National Ministry of Education
Shaanxi Key Laboratory for Advanced Energy Devices
Shaanxi Engineering Lab for Advanced Energy Technology
School of Materials Science and Engineering
Shaanxi Normal University
Xi'an 710119, China
E-mail: Zhaok@snnu.edu.cn
The ORCID identification number(s) for the author(s) of this article can be found under https://doi.org/10.1002/adma.201903889.

DOI: 10.1002/adma.201903889

yet inevitable, even in the optimal condition, causing electrical field-dependent charge extraction and reduction of fill factor (FF) in 2D PSCs.[24–26] Besides, due to the presence of multiple phases and complexity of carrier transport networks in $BA_2MA_3Pb_4I_{13}$, larger voltage losses (compared to single phase-dominant 3D PSCs) related to charge recombination or/and inefficient charge extraction are often encountered, limiting the PCE.[24] Therefore, improving the molecular arrangement and phase alignment in 2D perovskites is critically important for further enhancing the efficiency in RP phase 2D PSCs. To date, the fundamental understandings on these aspects are still under active debate.[27] A prototype structural model for RP-phase 2D perovskites constitutes a major phase (with a fixed *n*-value) associated minor phases that tend to have a random distribution in the bulk film.[8,10] Within this framework, it is believed that the excitons are primarily generated within the major 2D phases and dissociated carriers are then transported along the minor (e.g., 3D phase) in BA based solar cells.[28] Recently, a couple of studies have highlighted the presence of multiple phases (n: $1-\infty$) in 2D perovskites along out-of-plane (vertical) orientation when cast from single-phase precursors with a fixed stoichiometric *n*-value. In principle, such phase distribution will benefit the carrier transport/extraction in 2D PSCs with the formed energetic cascades.[13,29,30] However, how this proposed phase arrangement impacts realistic photovoltaic characteristics in 2D PSCs is not fully understood. Moreover, effective control on the phase distribution in 2D perovskites is challenged by the commonly adopted spin coating and rapid crystallization (e.g., fast annealing). To this end, seeking delicate management on the vertical phase alignments to improve charge sweepout and reduce recombination losses is a key to further boosting the PCE in 2D PSCs.

In this paper, we present a proof-of-principle study through proposing a slow post-annealing (SPA) method for 2D PSCs based on $BA_2MA_3Pb_4I_{13}$ photo-absorbers. Coupled with hot-film deposition, the ultimate PCE in SPA-treated PSC is boosted to 17.3%, showing a simultaneously enhanced open-circuit voltage (V_{oc} = 1.24 V) and a short-circuit current (J_{sc} = 19.86 mA cm^{-2}). Intensity investigations with photoluminescence (PL) and transient absorption (TA) spectroscopy alongside surface analysis indicate that fine gradients in vertical distribution of multiple perovskite phases (from the 2D phase, n = 1 in the bottom to quasi-3D phase, $n = \infty$ near the top region) are obtained with SPA, leading to favorable alignment on the bandgap energy in the 2D perovskite. The results of XRD and GIWAXS evidence that an improved crystal orientation is obtained in the 2D perovskites treated with SPA. These modifications lead to boosting charge transport and extraction with reduced Shockley–Read–Hall (SRH) recombination in the solar cells, revealed by transient electrical measurements. To the best of our knowledge, the achieved PCE is the one of the highest efficiencies reported on 2D PSCs based on BA organic spacers (n = 4) so far. Advantageously, the stability of SPA-processed devices is satisfactorily maintained, showing <4.5% degradations after 2000 h under N_2 environment without encapsulation. The demonstrated process strategy provides a promising route for improving the performance in 2D PSCs toward realistic applications.

In this study, the solar cells based on $BA_2MA_3Pb_4I_{13}$ photo-absorbers were fabricated with a p–i–n structure of indium-tin-oxide (ITO)/poly(triaryl amine) (PTAA)/perovskite/C_{60}/BCP/Ag (see illustrated device architecture in Figure S1 in Supporting Information). The energy diagram of $BA_2MA_3Pb_4I_{13}$ perovskites near the surface alongside utilized charge transporting layers is illustrated in **Figure 1**a based on the results of ultraviolet photoemission spectroscopy (UPS, see Figure S2, Supporting Information) and optical absorption. The PTAA and C_{60}/BCP served respectively a hole transporting layer and an electron transporting/hole blocking layer in our devices.[19] The photoactive layers were fabricated in ambient air atmosphere. The key process of SPA for the $BA_2MA_3Pb_4I_{13}$ PSCs involved thermal annealing of the finished devices at 60 °C continuously for 60 h in a N_2-protected environment. As a result, rearrangement of the vertical distribution in multi-perovskite phases was realized during the SPA process.

To demonstrate the impact of the SPA on the photovoltaic performance, we concerned four processing conditions, including room-temperature (RT) casting/no SPA, hot-casting/no SPA, RT-casting/SPA, and hot-casting/SPA. The optimization of SPA was established through screening different SPA treatment temperatures and time for $BA_2MA_3Pb_4I_{13}$ solar cells (see results in Figures S3 and S4 in the Supportng Information). We found that application of SPA at 60 °C for 60 h yielded the best efficiency improvement. Therefore, all the analyses involving SPA below are based on the optimal condition (60 °C/60 h) unless stated elsewhere. Figure 1b shows cross-section SEM image of a $BA_2MA_3Pb_4I_{13}$ solar cell with SPA treatment where the interfaces between different layer components are well resolved. Representative current density versus voltage (J–V) characteristics under AM 1.5 G solar irradiation (100 mW cm^{-2}) are shown in Figure 1c for 2D PSCs with various film processing. From the extracted device parameters (**Table 1**), considerable enhancements on the three parameters are observed in the SPA-treated devices. For example, the V_{oc} and PCE increase from 1.08 to 1.21 V and from 12.2% to 15.66%, respectively in the RT-cast device with SPA. Remarkably, combining hot-casting and SPA, the J_{sc} and V_{oc} are simultaneous boosted, reaching J_{sc} = 19.86 mA cm^{-2} and V_{oc} = 1.24 V. These improvements lead to achieving a champion PCE of 17.26%, which to the best of our knowledge is the highest reported efficiency in 2D PSCs based on BA organic spacers (n = 4). [8,10,12,19]

It is noted that in the champion cell the hysteresis effect is negligible, reflected by the nearly overlapped J–V characteristics at different scan directions (Figure 1c). To quantify this merit,

Table 1. Device parameters of best $BA_2MA_3Pb_4I_{13}$ 2D-PSCs in different film processing conditions.

Film processing	Scanning direction	V_{oc} [V]	J_{sc} [mA/cm^2]	FF [%]	PCE [%]
RT-casting/no SPA	Reverse	1.07	16.80	67.60	12.20
Hot-casting/no SPA	Reverse	1.08	18.49	68.21	13.62
RT-casting/SPA	Forward	1.20	17.06	75.83	15.56
	Reverse	1.21	17.09	76.16	15.66
Hot-casting/SPA	Forward	1.21	19.89	70.83	17.10
	Reverse	1.24	19.86	70.44	17.26

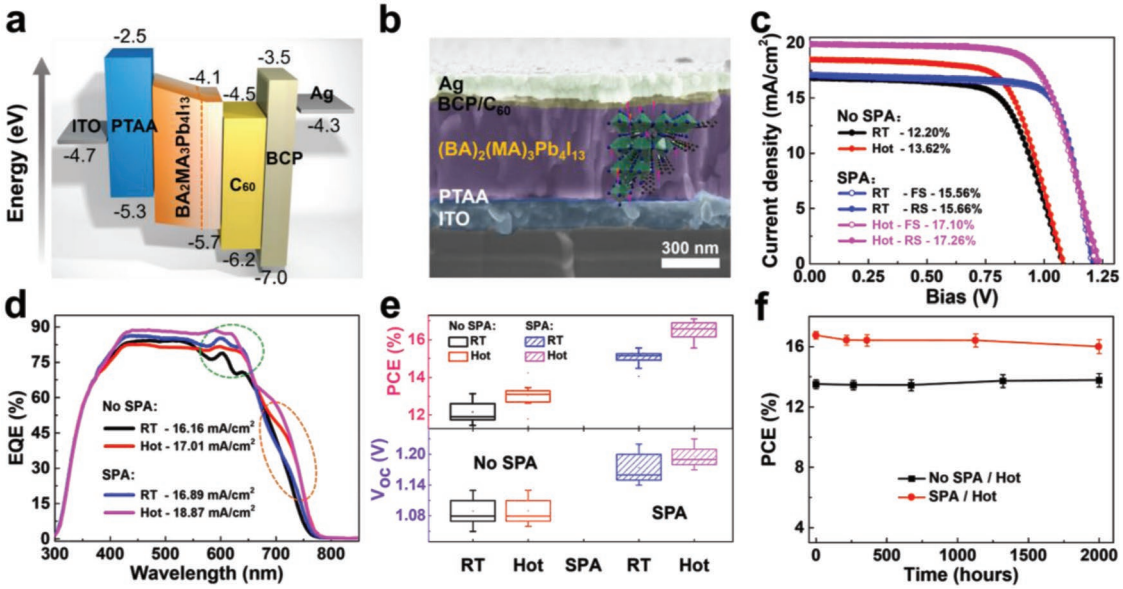

Figure 1. a) Energy diagram of 2D $BA_2MA_3Pb_4I_{13}$ perovskite alongside utilized charge transporting layers with the values for perovskite extracted from UPS and optical absorption measurements. b) Cross-section scanning electron microscopy image of a 2D perovskite solar cell (PSC) based on $BA_2MA_3Pb_4I_{13}$ photo-absorber treated with SPA. Embedded picture illustrates the lattice structures of multiple perovskite phases along the film growth direction. c) Current density versus voltage (*J*–*V*) characteristics of various $BA_2MA_3Pb_4I_{13}$ PSCs under AM 1.5 g solar irradiation (100 mW cm^{-2}). Inset text: extracted power conversion efficiencies (PCE). d) External quantum efficiency spectra of according devices together integrated short-circuit currents (inset text). e) Photovoltaic parameters of PCE and V_{oc} based on $BA_2MA_3Pb_4I_{13}$ solar cells (20) with different film processing. f) PCE together with error bars of pristine and SPA-treated 2D PSCs (hot-cast) as a function of storage time under N_2 environment without encapsulation.

we calculated the hysteresis index (HI) according to the relation described previously.[19] The devices with SPA are associated with lowered HIs of 0.007 (RT-cast film) and 0.008 (hot-cast film) which are much smaller than those of representative high efficiency 3D PSCs.[31–34] The reduced hysteresis can be attributed to a minimization of ion motion or surface charge trapping (e.g., by iodine or metal ions) with the described SPA processing,[35,36] which enables to fabricate high efficiency 2D PSCs with a good operational stability.

To better understand the enhanced J_{sc} with SPA, we compared external quantum efficiencies (EQE) of different solar cells with the results shown in Figure 1d. For the compared four devices, the J_{sc} based on the integration of EQE exhibits deviations <5% with respect to the values extracted from *J*–*V* characteristics. On top of the overall higher EQE in the SPA-treated device, a spectral difference is found in the low energy region where the photocurrent originates from the absorbed photons in 3D or higher *n*-value components.[29] In this region, we note a pronounced EQE shoulder centered around 750 nm in the SPA-treated devices. As will be further clarified, this shoulder could be related to the modified vertical phase gradients during SPA, such that charges (electrons) arising from low-energy photons absorbed by the perovskite active layer are more effectively transported toward the cathode, eventually contributing to the increase of photocurrent. Apart from the EQE shoulder, more flattened EQEs in the 400–600 nm range are observed in the champion cell. All these results suggest the reduction of photocarrier losses in the devices modified with SPA.

Figure 1e presents the statistics of photovoltaic parameters of PCE and V_{oc} with different film processing (see statistics of all the photovoltaic parameters in Figure S5, Supporting Information). On average, the PCEs based on SPA treatment are enhanced to 15.20 ± 0.817% and 16.58 ± 0.574% for the RT- and hot-cast devices, respectively. Physically, the V_{oc} is related to the losses via radiative recombination (due to spectral mismatch) and non-radiative ($V_{non\text{-}rad}$) recombination involving traps or interfacial misalignment.[19] In a recent study, it has been argued that the V_{oc} in 2D PSCs is mainly limited by the bandgap of 3D-like phases.[28] Given that the optical bandgap of our 2D perovskites remains nearly affected after SPA, all amounting to ≈1.6 eV (see Figure S6, Supporting Information), the enlargement of V_{oc} can be primarily ascribed to the reduced non-radiative recombination in the SPA-modified perovskite films, such that the voltage loss via $V_{non\text{-}rad}$ becomes mitigated. As discussed below, the enlarged V_{oc} also can arise from the modified phase distribution in the perovskite active layer with SPA, leading to minimizing the interfacial energy misalignment between the perovskite and cathode.

With the achieved enhancement on the photovoltaic efficiency, we examined the stability in these $BA_2MA_3Pb_4I_{13}$ devices by tracking the PCE decay as a function of storage time (see results in Figure 1f). To simplify our comparison, all devices were kept in a N_2-protected atmosphere (without encapsulation) to minimize the oxidization of Ag electrodes and damages of perovskites by O_2 and H_2O in air .[37,38] As can be seen, the SPA-treated solar cell exhibits a similar decay tendency as in the control devices. It is remarkable that both of the efficiencies remain above 96% of initial ones after storing the devices for ≈2000 h. The satisfactory long-term stability in the 2D PSCs mainly originates from the suppressed ion draft in the presence of hydrophobic BA spacers.[13,27]

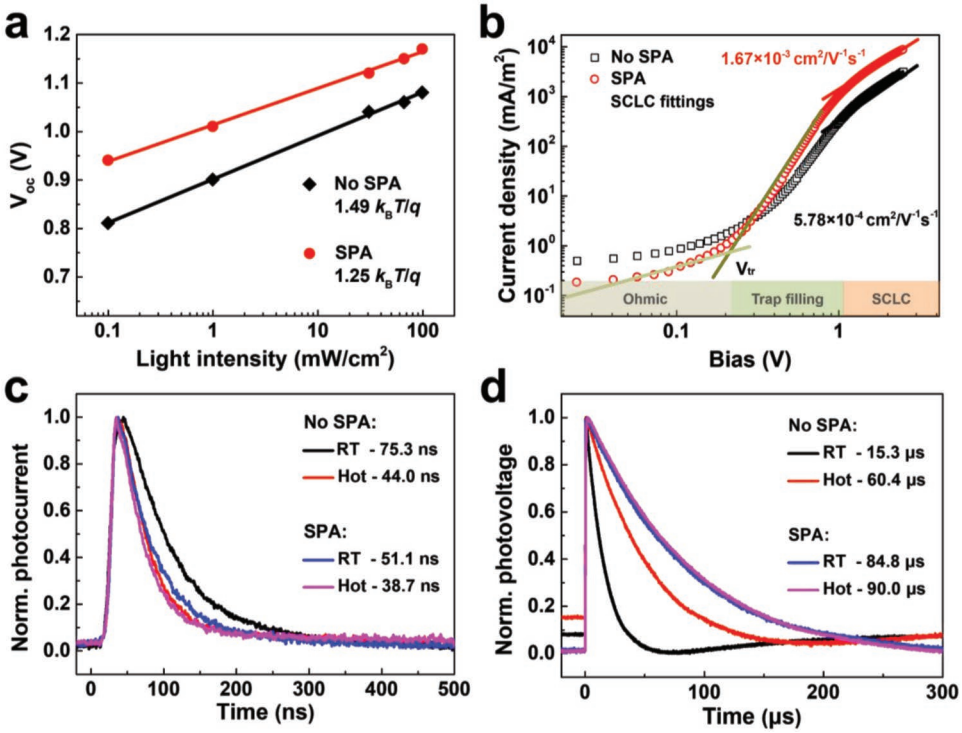

Figure 2. a) Open-circuit voltage (V_{oc}) versus light intensity characteristics of hot-casting $BA_2MA_3Pb_4I_{13}$ solar cells before and after SPA treatment. Inset text: determined slopes in terms of thermal voltage (k_BT/q) based on linear fittings. b) Dark *J–V* characteristics of electron-only devices based on pristine and SPA-treated 2D perovskite active layers (hot-cast). Also included are the determined electron mobility and the extracted transition voltages (V_{tr}) from the ohmic current to trap-filling current in respective conditions. c) Transient photocurrent and d) transient photovoltage decay kinetics measured on 2D PSCs in different film processing conditions.

To obtain solid evidence on the reduced charge recombination and facilitated charge extraction with SPA treatment, we carried out light intensity (P_{light})-dependent *J–V* measurements shown in Figure S7 in the Supporting Information. The diode ideality factor (IF) was determined from the slope of V_{oc} versus P_{light} plot, which was exhibited in **Figure 2**a. Generally speaking, a slope approaching $2k_BT/q$ with IF = 2 (k_BT/q is the thermal voltage) refers to a dominant SRH recombination process involving traps.[39–41] When the slope reduces to $1k_BT/q$ with IF = 1, it means that the second order bimolecular recombination plays a more significant role.[41] In our case, the extracted slopes amount to $1.49k_BT/q$ and $1.25k_BT/q$ for the pristine and SPA-processed devices (both with hot-film casting). The reduced IF unambiguously confirms the suppression of SRH charge recombination in the SPA-treated PSC. Figure S8 in the Supporting Information shows J_{sc} versus P_{light} characteristics of pristine and SPA-modified devices. The relation between these two parameters obeys the general power law as $J_{sc} \propto P_{light}^{\alpha}$ with the power α being an exponential factor.[40,41] In the solar cell where the recombination adopts the monomolecular path, the power should approach unity.[41] Based on linear fittings, we extracted an α value of 0.97 and 0.93 for the pristine and SPA-treated devices, respectively. The slightly reduced α is consistent to that the SPA modification leads to suppressing monomolecular recombination in our 2D PSCs.

To have a quantitative assessment on the density of traps (N_{trap}) that can serve non-radiative recombination centers in operational devices,[19,42] we fabricated electron-only devices based on the same set of 2D perovskite films. As seen from the *J–V* characteristics shown in Figure 2b, we observe a clear transition from the linear behavior at low voltages (ohmic region) to the trap-filling current (TFC) region characteristic of a stronger voltage dependence. Upon further increasing the bias, the quadratic voltage dependence appears, commonly described by the space-charge-limited current (SCLC). Based on the voltage (V_{tr}) at which the transition from the linear transport to TFC occurs, N_{trap} was determined by using the relation expressed as[42,43]

$$N_{trap} = \frac{2\varepsilon_0 \varepsilon V_{tr}}{qL^2} \quad (1)$$

where ε_0 is the vacuum dielectric constant, ε_r is the relative dielectric constant of perovskites (≈25),[25] q the elemental charge and L the thickness of the active layer. The determined N_{trap} reduces to 3.47×10^{15} cm^{-3} with hot-casting/SPA, compared to a N_{trap} of 6.76×10^{15} cm^{-3} in the device without SPA (hot-cast). Similar trend in the reduction of N_t is found based on the analysis of dark current of solar cells (Figure S9, Supporting Information). The reduction of N_{trap} should benefit the reduction of non-radiative SRH recombination.[19,37] In the ohmic region, the dark current density (J_0) of the SPA-processed electron-only device (or solar cells, see Figure S9, Supporting Information) reduces with respect to that without SPA. It hints that the population of background carriers, possibly arising

from under-coordinated ions decrease[44] leading to a higher diode quality.

To shed more light on charge transport properties influenced by SPA, we assessed the electron mobility (μ_e) in the perovskite active layer with single-carrier device measurements (see details in the Experimental Section). The obtained dark *J*–*V* characteristics of $BA_2MA_3Pb_4I_{13}$ single-carrier devices are displayed in Figure 2b. After SPA treatment, the electron current in the SCLC region visibly increases, suggesting the enhanced μ_e of mobile carriers. Through fittings with the Mott–Gurney law,[45] the μ_e was determined to be 5.78×10^{-4} cm^2 V^{-1} s^{-1} (without SPA) and 1.67×10^{-3} cm^2 V^{-1} s^{-1} (with SPA) showing a twofold enhancement. The improved charge transport with SPA favors the sweepout of photocarriers in operational devices which primarily arises from the modified phase arrangement and increased crystallinity in the 2D perovskite, as will be addressed in follows.

In light of the enhanced transport and mitigated SRH recombination, we expect more rapid charge extraction accompanied with retardation of charge recombination. To verify this, we performed transient photocurrent (TPC) and photovoltage (TPV) measurements on these solar cells with the results displayed in Figure 2c,d. Consistently, the devices with SPA treatment exhibit speedier charge sweepout with shortened charge extraction time (τ_{ext}) at short-circuit condition (Figure 2c). The shortest τ_{ext} of 38.7 ns was found in the champion devices, followed by that with the RT-casting/SPA devices (τ_{ext} = 51.1 ns), then the hot-casting/no SPA devices (τ_{ext} = 44.0 ns), and lastly the RT-casting/no SPA devices (τ_{ext} = 75.3 ns). The enhanced charge extraction efficiency minimizes interfacial charge accumulation and resultant carrier loss via recombination, which reconciles the enlarged J_{sc} and V_{oc}.

The recombination lifetime (τ_{rec}) in operational solar cells was determined by TPV measurements in the open-circuit condition (Figure 2d). In this situation, the net current flow is zero and the τ_{rec} reflects the lifetime of photocarriers.[46,47] Based on a mono-exponential decay model, considerable elongations of τ_{rec} were identified in the devices with SPA, from τ_{rec} of 15.3 and 60.4 µs without SPA to 84.8 and 90.0 µs after SPA for RT and hot-cast devices, respectively. These results well agree to respective solar cell parameters. Based on previous studies, the ratio of τ_{ext} to τ_{rec} was found relevant to the FF in solar cells.[46–48] Upon establishing an equilibrium between charge extraction and recombination during cell operation, decreasing the ratio of τ_{ext} to τ_{rec} allows for shifting the equilibrium toward the former process, which is favorable for the reduction of carrier losses and increase of FF. In our devices, the ratios of τ_{ext} to τ_{rec} reduce from 4.9×10^{-3} (no SPA) to 6.0×10^{-4} (after SPA) and from 7.3×10^{-4} (no SPA) to 4×10^{-4} (with SPA) based on RT- and hot-casting films, respectively. On this basis, the enlargement of FF with SPA result from the modified photophysical processes in a manner that the sweepout of photocarriers expediates and recombination retards.

As aforementioned, charge transport/extraction in 2D PSCs are affected the mixed perovskite phases and resultant energy alignment. In the SPA process, we speculate that the applied thermal energy prompts the migration of MA cations toward the cathode,[49] leading to adjustment on the phase arrangement and bandgap energy alignment in the photoactive layer. To enable in-depth insights into this process, we performed steady-state PL spectroscopy on $BA_2MA_3Pb_4I_{13}$ films with different processing. The PL was measured in two excitation configurations with the light incident on the top or bottom side of tested samples, which enables to acquire information relevant to different depths inside the photoactive film. As shown in **Figure 3**a, the PL of the two films (RT- and hot-casted) without SPA exhibits multiple peaks at different wavelengths (details for the peak positions corresponding to different *n*-values are shown in Figure S10 in the Supporting Information). This feature is suggestive of the presence of multi-perovskite phases in different *n*-values after rapid crystallization, which agrees with recent studies.[29] With RT-casting/no SPA, the peaks assigned to $n = 2$, 3, 4, and to $n = \infty$ phases are all observable, no matter of the top or bottom excitation. It indicates that the phase distribution in the upper and lower regions of $BA_2MA_3Pb_4I_{13}$ film does not differ significantly and the 2D and 3D components seem to be randomly interlaced throughout the whole bulk film.[13]

Differently, the PL with hot-casting/no SPA is dominated by the primary 3D phase peak (740 nm) when measured from the top side, while stronger peaks of 2D phases with respect to the 3D phase are observed in the bottom-excited PL. From these observations, we can conclude that a vertical phase separation in the order of *n* tends to occur from the bottom toward the top regions inside the perovskite. This feature can be understood in terms of the thermal energy applied to the substrate that provides a driving force for phase separation during film drying.

Upon application of SPA (see Figure 3b), the PL corresponding to the lower-*n* phases (hot-cast film) become more observable with top excitation, compared to that with hot-cast/no SPA. Between the two SPA-processed films, we note a broadened PL at higher-*n* (or 3D like) phases with hot-casting. This could be connected to an enlarged phase multiplicity near the top region of perovskite films. When excited at the bottom, it is consistent that the PL intensities of 2D phases considerably enlarge relative to the 3D phase peaks (with both RT- or hot-casting), indicating the enhanced crystallization of 2D phases in the bottom area of perovskites after SPA. With these observations, it is likely that the SPA adjusts the distribution of multi-perovskite crystal phases in a more gradual fashion along the direction normal to the film surface.

To further verify that the specific phase alignment in the SPA-treated 2D perovskite films, we performed incident angle-dependent PL spectroscopy with bottom excitation (see Figure 3c and Figure S11 in the Supporting Information). The light penetration depth decreases with the increase of incidence angle such that the obtained fluorescence signal can reflect changes in the composition from the bottom toward the top regime inside the film. As shown in Figure 3c, the relative PL intensity corresponding to the $n = \infty$ phase decreases with the increase of incident angle, indicating that the population of 3D perovskite phase with hot-cast/SPA processing gradually increases from bottom toward the top area. Differently, we observe more random tendencies in the relative changes of 3D-like peaks in the other three films, particularly in the case with RT-cast/no SPA processing. The results strongly indicate an improved vertical phase alignment along the direction of film growth in the order of *n*-values.

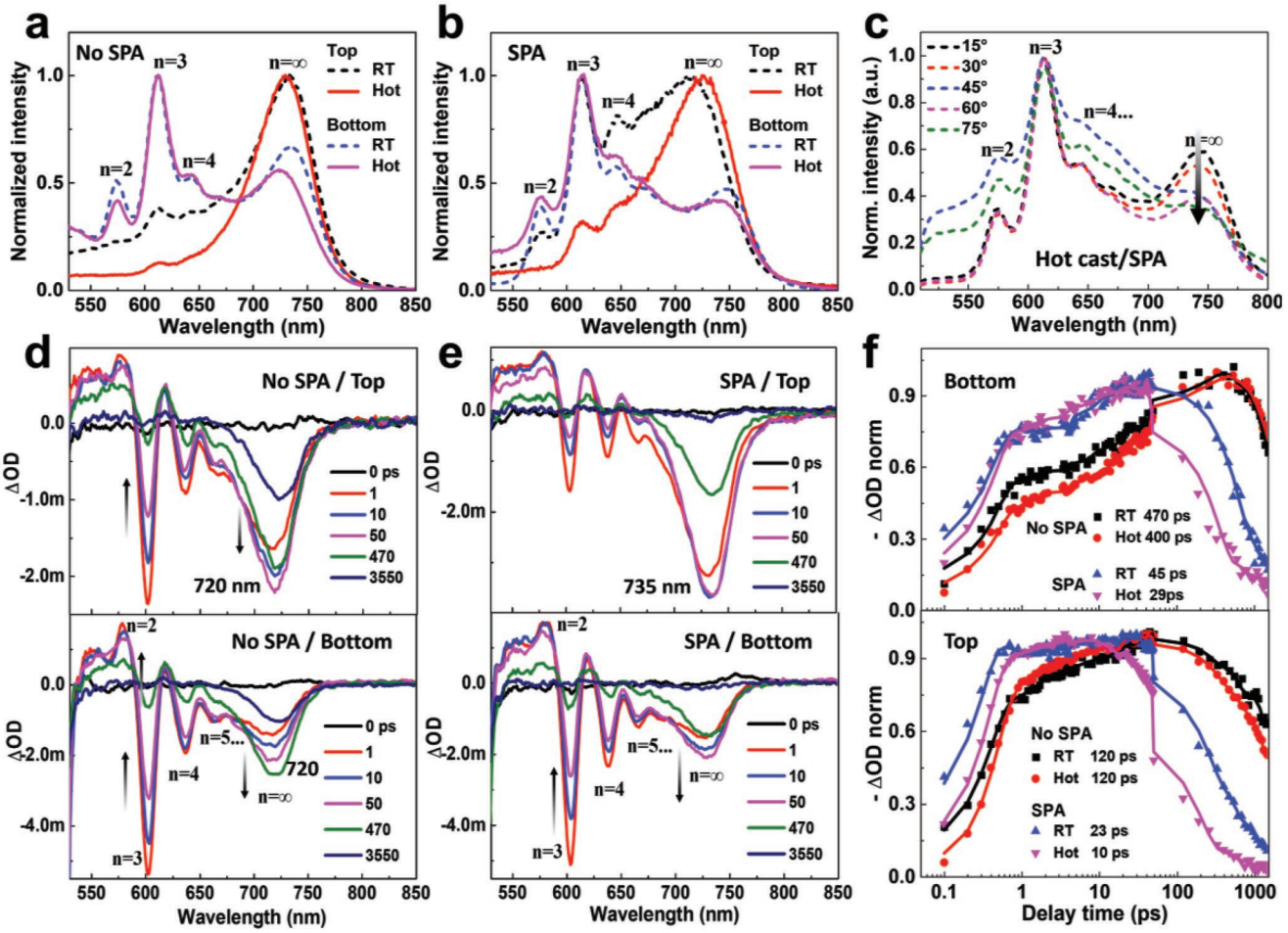

Figure 3. Steady-state photoluminescence (PL) spectroscopy based on pristine a) and b) SPA-treated $BA_2MA_3Pb_4I_{13}$ perovskite films in top and bottom excitation configurations. c) Incidence angle-dependent steady-state PL spectra measured on a hot-cast 2D perovksite film with SPA treatment (bottom excitation). Transient absorption (TA) spectra at different time delays of RT-cast $BA_2MA_3Pb_4I_{13}$ films d) without SPA and e) with SPA treatment in different excitation configurations. f) TA kinetics probed at $n = \infty$ bleach peaks based on different 2D perovskite films under b) bottom and c) top excitations.

We further measured time-resolved PL spectroscopy on these 2D perovskite films based on ITO/PTAA substrates (see results in Figure S12, Supporting Information). We observe two temporal regimes in the PL decay kinetics where the fast and slow decays can be related to the surface conditions and bulk films, respectively. With SPA, the decay time considerably decreases (RT-cast films: $\tau_1 = 4.29$ ns, $\tau_2 = 15.95$ ns versus after SPA: $\tau_1 = 0.43$ ns, $\tau_2 = 3.74$ ns; hot-cast films:$\tau_1 = 3.88$ ns, $\tau_2 = 16.02$ ns versus after SPA: $\tau_1 = 0.37$ ns, $\tau_2 = 3.60$ ns). In the presence of PTAA, the shortened decay time in the fast decay regime is in line with promoted hole transfer through PTAA to the anode.[19] The shorter-lived PL with SPA is also explained by the increased accumulation of lower energy 2D phases accumulated in the bottom area (according to the results of Figure 3a,b), such that the hole transfer can be prompted through these 2D phase perovskites.[29] This feature is beneficial for the increase of FF in PSCs with reduced interfacial charge recombination.[50] In the slower decay region, the decay time can be correlated to the general picture of exciton migration from higher energy to lower energy sites.[8] In the SPA-treated film, the considerably decreased decay time in this temporal region implies that the migration/transfer between different perovskite phases are promoted by the formed energetic cascades.[29]

To establish clearer correlations of the enhanced device performance to the phase alignments in $BA_2MA_3Pb_4I_{13}$ perovskites, we performed femtosecond TA spectroscopy (excitation light: 500 nm, 2.57 μJ cm^{-2}). As shown by the characteristics of differential transmittance (ΔOD) versus wavelength of TA (see Figure 3d,f for RT-cast films and Figures S13 and 14 in the Supporting Information for hot-cast films), the TA spectra based on different film processing and excitation configurations are featured by the ground state bleaching (GSB) peaks corresponding to the phases of $n = 2$, 3, 4, 5, and ∞.[29] Notedly, within the first 50 ps, the evolution of the reducing GSB signals assigned to lower-n phases (at higher energies) is accompanied with the augmentation of GSB peak at $n = \infty$ (730 nm). This behavior can be interpreted by the charge transfer from the higher energy (lower-n) phases to $n = \infty$ phase in 2D perovskites.[29,51] Through comparing the TA decay kinetics of different perovskite phases (see Figure S15, Supporting Information), we find

that the decay time of higher-energy peaks (2D phases) considerably shortens compared to that of the lower-energy peak (e.g., for $n = \infty$). This trend agrees with the PL decay kinetics, revealing the exciton transfer from high-energy states to low-energy states in the 2D perovskites with multiple phases.[51]

Through comparing the TA peak intensities (Figure 3f) at selected time delays. deepened insights into the modified phase distribution in the 2D perovskites are gained. For the film with RT-casting/no SPA, the overall GSB intensities at different probing time (up to a few nanoseconds) are more comparable between the lower-*n* and 3D phases with both top- and bottom-excitations. Contrastingly, with SPA treatment the intensities of TA peaks for lower-*n* phases significantly decrease (top-excitation) while the peak intensity ratios of the smaller-*n* phases to $n = \infty$ phase reverse (bottom excitation). These observations agree with the reduction of 2D components near the top area and more dominant lower-*n* phases in the bottom region in the SPA-processed film. Regarding the TA signals of 3D phases, a red-shift (from 720 to 735 nm) is noted, which further affirms the accumulation of 3D phase or/and higher-*n* components near the top area. The combined results of TA and PL strongly indicate that the slowly applied thermal energy during SPA modifies the crystallization kinetics of the $BA_2MA_3Pb_4I_{13}$ films that finer phase gradients in the order of *n* along the direction normal to the substrate could be realized. With an energetic standpoint, such gradient phase distribution favors the vertical bandgap energy alignment for carrier transport, which reconciles the enhanced carrier mobility/charge extraction in the PSC.

Based on the TA spectra, we further explored the TA dynamics probed at different energies corresponding to different phases (Figure S15, Supporting Information). At early time pieces, a rising of TA kinetics in respective bands is observed, reflecting the populating at this phase.[29] Of note, the TA rising time assigned to different phases exactly follows the order in *n*-values, i.e., the signal of lower-energy phases is associated with a slower rising or vice versa. This tendency is in line with the scenario that the carrier transport in these 2D perovskites involves electron (or energy) transfers from lower-*n* phases to 3D phase. In **Figure 4**f, we compared the TA kinetics probed at the $n = \infty$ (720 nm) band for different $BA_2MA_3Pb_4I_{13}$ films. With bottom excitation (upper panel in Figure 4f), the rising kinetics are much faster for the SPA-treated films, yielding a shorter carrier populating time of 45 ps (RT-cast) and 29 ps (hot-cast), versus 470 ps (RT-cast) 400 ps (hot-cast) without SPA. This result indicates the more efficient electron transfers from the lower-*n* to $n = \infty$ phases after SPA treatment,[29,51] benefitted from the modified band energy alignment. The same trend is observed using top-excitation that the rising of the TA signals at $n = \infty$ band becomes speedier (lower panel, Figure 4f). These changes in TA kinetics with SPA well agrees with the enlarged electron mobility and charge extraction efficiency in according 2D PSCs.

With the identified modification on the phase distribution and resultant energetic alignment with SPA, we examined the crystallinity by X-ray diffractometry (XRD). Figure 4a shows XRD patterns of $BA_2MA_3Pb_4I_{13}$ films with different processing. The XRD peaks in $BA_2MA_3Pb_4I_{13}$ are dominated by the (111) and (202) facets, consistent to previous results.[8,10] We also evaluated the full width at half maximum (FWHM) of the (202) peaks for different perovskite films. As shown in Figure 4a Inset, reduced FWHMs of 0.188° (RT-cast) and 0.177° (hot-cast) are found for the SPA-processed films, compared to FWHM = 0.228° (RT-cast) and 0.206 (hot cast) without SPA. It suggests that the slow annealing further enhances the crystallinity of $BA_2MA_3Pb_4I_{13}$ films. Based on XRD, the average crystal size of 202 facet was determined based on the Scherrer formula.[52] Of note, the D_{202} increases to 47.7 nm (RT-cast) and 50.6 nm (hot-cast) after SPA. The indicated enlargement of crystal sizes may reduce the number of grain boundaries

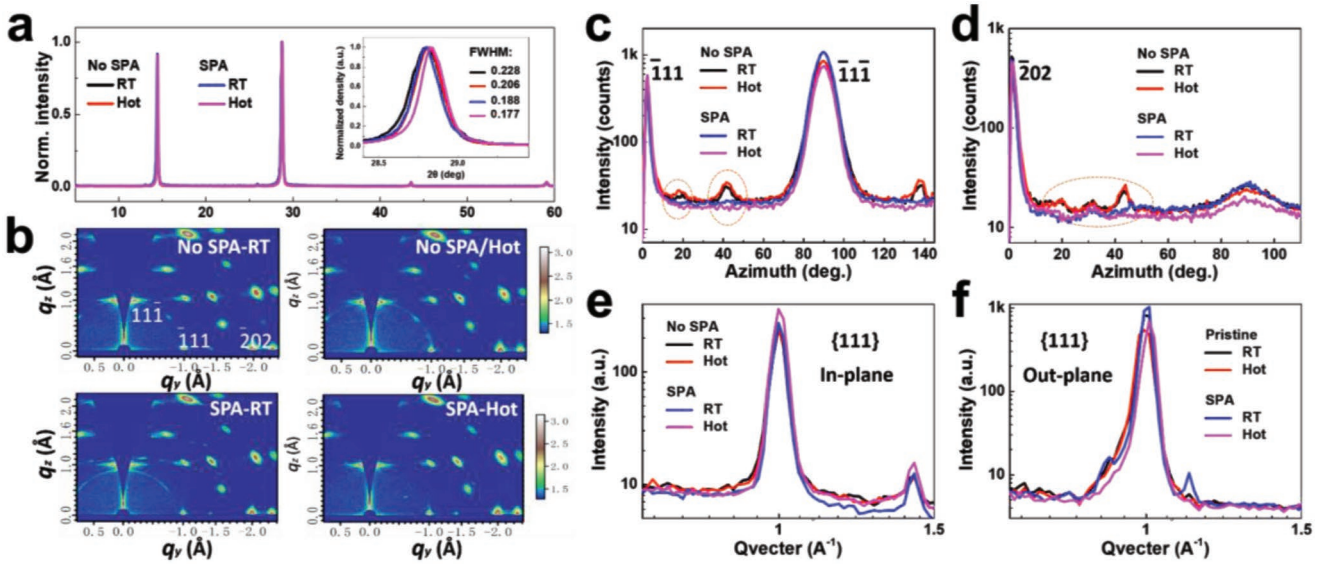

Figure 4. a) X-ray diffractometry of $BA_2MA_3Pb_4I_{13}$ films prepared on PTAA substrates with calculated FWHMs for the (202) facets. b) 2D GIWAXS patterns of $BA_2MA_3Pb_4I_{13}$ perovskite films with different processing. Azimuth integral curve of $BA_2MA_3Pb_4I_{13}$ at c) {111}, and d) {202} planes. Line-cut profile curves of 2D GIWAXS along e) in-plane directions and f) out-of-plane for the stacking of {111} plane.

and structural defects.[8,26] Moreover, the surface cracks induced by hot-film deposition are healed after SPA treatment with the surface becoming much smoother, as evidenced by the scanning electron microscopy images in shown in Figure S16 in the Supporting Information. All these morphological modifications favor the suppression on trap-assisted charge recombination in 2D PSCs.[53,54]

To explore the molecular stacking orientations affected by SPA, grazing incidence wide-angle X-ray scattering (GIWAXS) was performed on different $BA_2MA_3Pb_4I_{13}$ films and the 2D GIWAXS patterns are shown in Figure 4b. All the films exhibit discrete Bragg spots along the same rings, indicating that, the crystal domains in our polycrystalline 2D perovskites are mainly oriented with their (101) planes parallel to the substrate surface.[10] For the films without SPA, the diffraction rings display weaker scattering intensities along certain extended arc segments, suggesting a higher randomness in the crystal orientation.[10,19] After SPA, sharper discrete Bragg spots are observed and this feature can be attributed to the more ordered crystal arrangement developed during the SPA process. The increased ordering in crystal arrangement along the direction parallel to the substrate facilitates the charge transport in 2D PSCs. The modified crystal orientation of the (111) and (202) planes in the SPA treated sample can be manifested by the Azimuth integral curve shown in Figure 4c,d. For the film without SPA, we observe a broader Azimuth distribution for the probed two crystal planes with the scattering peaks at 20° and 40° becoming observable. This point to the fact that the crystal orientation is more random. In contrast, for the SPA-treated films, the (111) crystal plane stacking orientation is found only at 0° and 90° and the peak assigned to the $(\bar{2}02)$ stacking orientation only appears at 0° The dominant in-plane (IP) stacking of the $\bar{2}$ 0 2 facets points to an important fact that the (202) crystal facets are oriented parallel to the substrate (see schematics in Figure S17 in the Supporting Information). This structural feature can facilitate charge transport in the 2D perovskite films.

To assess the ordering in the stacking of crystallographic planes, we further calculated the crystal correlation length (CCL) by using the following relation[19]

$$\mathrm{CCL} = \frac{2\Pi K}{\Delta q} \tag{2}$$

where Π is the ratio of circumference to diameter, k is a constant (here a value of 0.9 is used), and Δq is the FWHM of the diffraction peak. FWHMs were obtained by the gaussian fittings. Based on the GIWAXS line-cut profile curves shown in Figure 4e,f, the (111) planes with the RT-cast/SPA treatment presents an IP CCL of 16.62 nm and an OOP CCL of 21.74 nm. In comparison, the CCL in the film with RT-cast/no SPA reduces to 14.87 and 17.66 nm in the IP and OOP directions, respectively. The same trend was found for the hot-cast films without SPA. The increased CCLs suggest the formation of highly ordered crystals afforded by SPA treatment which is consistent with results discussed earlier.

We also examined surface contact potential (SCP) in these 2D perovskite films by Kelvin probe force microscopy. As seen from the SCP mapping in Figure S18 in the Supporting Information, uniform features are observed in all samples, implicative of a homogeneity of phase distribution in the lateral direction. Based on averaging the SCP values, an elevated surface work function (WF) in the SPA-processed film was identified. Given the energetic differences between 2D and 3D components, the reduced WF can be attributed to the rearrangement of perovskite phases with a 3D phase-rich surface. The shifted WF is consistent to the higher valence band in $BA_2MA_3Pb_4I_{13}$ films with SPA determined by UPS (from 5.74 eV without SPA to 5.50 eV with SPA, see Figure S2, Supporting Information). The results of KPFM affirm the reorganization of the multiple perovskite phases in $BA_2MA_3Pb_4I_{13}$.

It is noteworthy that the applied SPA treatment involves the whole device containing charge transporting layers. To understand the impacts of interfacial modification during the SPA treatment, we measured the efficiency of 2D PSCs for which the SPA was treated only on the perovskite layer (prior to the deposition of C_{60}). We found that the PCE after SPA increases from 13.62% to 15% (Figure S19, Supporting Information), less significantly compared to the results with applying SPA on the whole device. The moderately enhanced PCE with SPA in the absence of C_{60} hints that the incorporation of C_{60} layer atop the 2D perovskites during SPA is necessitated to achieve greater PCEs which may be related to i) a favored protection for 2D perovskites from excess exposure to the environment where SPA is applied and ii) a promoted modification on the surface properties in 2D perovskites by C_{60} during SPA. This latter is based on the consideration that C_{60} enables to passivate electron traps near the surface area perovskite films.[55,56] To affirm this, we fabricated 3D PSCs with $Cs_{0.05}(FA_{0.15}MA_{0.85})_{0.95}PbI_3$ absorbers and applied the same SPA procedure (by doing so, the influence of SPA on the phase alignment can be ruled out). As comparatively shown by the results in Figure S20 in the Supporting Information, the SPA-treated 3D PSC does yield an enhanced PCE (although the improvement is not considerable). These results point to the fact that surface trap passivation of 2D PSCs is likely promoted during the process of SPA in the presence of C_{60}, which partially attributes the enhancement of efficiency.

To gain a theoretical insight into the achieved phase alignment afforded by SPA, we performed first-principles density functional theory (DFT) calculations to evaluate the formation enthalpy of $(BA)_2(MA)_{n-1}Pb_nI_{3n+1}$ (n = 1,2,3...∞). The formation enthalpy is defined as the free energy difference between the precursors and target materials. The formation pathway of target materials was considered for the $(BA)_2(MA)_{n-1}Pb_nI_{3n+1}$ as following

$$\mathrm{MAI} + \mathrm{BAI} + \mathrm{PbI_2} \rightarrow (\mathrm{BA})_2(\mathrm{MA})_{n-1}\mathrm{Pb}_n\mathrm{I}_{3n+1} \tag{3}$$

As can be seen from the calculation results in **Figure 5**a, with the n-value decreasing from ∞ (bulk phase) to 3, 2, and 1, the ΔH_{for} values show a significant decrease from −0.01 to −0.2, −2.1, and −2.8 eV. This substantial reduction with lower-n value suggests more favored crystallization of $(BA)_2(MA)_{n-1}Pb_nI_{3n+1}$ materials with lower-n value in contrast to higher-n materials. This is fully consistent with the morphological and photophysical observations that lower-n phases are precipitated closed to the substrate with higher-n enriching near the film surface.

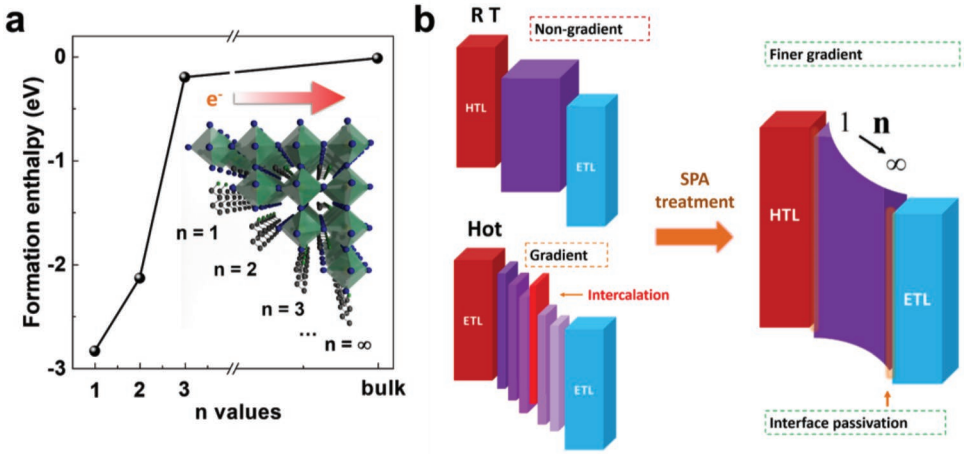

Figure 5. a) Proposed energetic distributions along the vertical orientation in 2D $BA_2MA_3Pb_4I_{13}$ perovskites with different film processing. b) Calculated formation enthalpy of $(BA)_2(MA)_{n-1}Pb_nI_{3n+1}$ (n = 1,2,3,...∞) materials from precursors by density functional theory. Inset graph: illustrated lattice structure and phase arrangement achieved with hot-casting/SPA processing.

On the basis of the combinatorial experimental analyses and theoretical calculation, at last we attempted to propose a model for the possible bandgap energy distributions in our 2D perovskite films in different processing conditions. As schematically illustrated in Figure 5b, the 2D and 3D phases without SPA tend to adopt staggered arrangements in the top and bottom regions inside the perovskite layer. When hot-casting is applied, more abrupt and non-uniform phase gradients may form, leading to populations of the 2D phases and 3D phase near the bottom and top areas respectively. In these two processing conditions, the crystallization occurs rapidly and the resultant quantum well energy barriers appear unavoidable, which induces unfavored recombination channels in the active layer and hinders the photovoltaic efficiency. In contrast, the described SPA process modifies the phase distribution in a slow fashion, leading to finer energy gradients along the vertical direction. Consequently, the potential barriers induced by quantum wells are effectively reduced, which promotes charge transport and extraction, eventually boosting the PCE in our solar cells. In addition, the SPA likely promotes the interfacial passivation of $BA_2MA_3Pb_4I_{13}$ in the presence of C_{60}, which synergistically minimizes the ion motion and surface charge trapping. We expect that the SPA process may apply to other types of 2D PSCs with multi-phase distribution to achieve improved photovoltaic performance.

To summarize, we demonstrate a highly effective processing methodology with SPA for modifying the photovoltaic characteristics in RP phase 2D PSCs based on $BA_2MA_3Pb_4I_{13}$. With this method, we achieve an impressively enhanced PCE of 17.26% which is one of the highest reported efficiencies in 2D PSCs based on BA organic spacers (n = 4). The combined results of steady-state and time-resolved optical spectroscopic measurements provide strong evidence that the multi-perovskite phases in $BA_2MA_3Pb_4I_{13}$ are favorably aligned in the order of n-values along the growth direction perpendicular to the substrate after SPA treatment, leading to mitigating the potential barriers induced by quantum wells. Moreover, the crystal orientation in the 2D perovskite films is effectively improved with SPA treatment, revealed by the results of GIWAXS. These modifications lead to boosting charge transport/charge sweepout with suppressed SRH recombination in the solar cells such that the efficiency gains. Importantly, the merits of environmental stability in 2D PSCs is maintained after SPA treatment, manifested the low PCE degradation (<4.5%) after storing the devices for 2000 h. without encapsulation. The described SPA process opens a promising venue to tackle with key figures of merits in emerging 2D RP phase perovskite solar cells toward realistic energy conversion applications.

Experimental Section

Solution Preparation and Device Fabrication: 0.85 M $BA_2MA_3Pb_4I_{13}$ precursor solution was prepared by dissolving MAI (99.5%, Xi'an Polymer Light Technology Corp), BAI (99.5%, Xi'an Polymer Light Technology Corp) and PbI_2 (99.9985%, Alfa Aesar) in *N*,*N*-dimethylformamide (DMF, 99.9%, Aladdin) with a molar ratio of 2:3:4. PTAA (Xi'an Polymer Light Technology Corp) was dissolved in toluene with a concentration of 2 mg mL^{-1}. ITO substrates were cleaned by sonication in water, acetone, and isopropyl alcohol sequentially and then dried in an oven before use. The cleaned substrates were treated by using a UV-O_3 oven for 15 min. The hole transporting layer was attained by spin coating the PTAA solution (chlorobenzene) with a spin rate of 6000 rpm for 30 s. The $BA_2MA_3Pb_4I_{13}$ active layer was prepared in an air atmosphere, For hot-cast devices, the substrates containing PTAA were pre-heated at 60 °C for 10 min, and then quickly transferred onto the chuck of a spin coater. Right after that, 60 µL of perovskite precursor solutions were applied and spun coated at 5000 rpm for 20 s. For the RT-spun-coat devices, the same spin procedure was used but on the ITO/PTAA substrates without heating. The finished $BA_2MA_3Pb_4I_{13}$ films were thermally annealed at 100 °C for 10 min in air atmosphere. Then 30 nm of C_{60} and 9 nm BCP were respectively deposited on top of the active layer by thermal evaporation. Finally, 80 nm of Ag cathode was evaporated through shadow masks under vacuum <1×10^{-4} Pa.

For the SPA treatment, the complete devices were placed on a hot plate at selected temepratures (e.g., 60 °C in the optimal condition) in a N_2-pruged glove box. Afterward the solar cells were annealed continuously without any disturbance. After 60 h, the devices were taken out from the hot plate and natually cooled in the glove box before testing.

For electron-only devices, 2.1% wt% SnO_2 aqueous solution was spun coated at 3000 rpm for 30 s on pre-cleaned ITO substrates, and

then placed on a hot stage (150 °C) for 30 min. The perovskite active layer was deposited with the same spin procudured used for solar cells, followed by evaporation of C_{60} and silver electrodes.

First-Principles Simulations: The plane-wave method in the framework of DFT was used as implemented in the VASP code. The projector augmented wave method was used to describe the interaction between ion cores and valence electrons. The van der Waals (vdW) interaction was described by the DFT-D3 correction. A Γ-centered *k*-point of $9 \times 9 \times 9$ for Brillouin zone sampling was generated using the Monkhorst–Pack scheme during calculations. The lattice parameter and atomic positions of all structures were relaxed until the total energy changes became $< 1.0 \times 10^{-5}$ eV and the maximum force component acting on each atom was less than 0.01 eVÅ^{-1}.

Characterization: J–V curve characteristics of $BA_2MA_3Pb_4I_{13}$ solar cells were measured by using a Keithley 2400 Sourcemeter under nitrogen atmosphere irradiated by a AAA solar simulator at 100 mW cm^{-2} using an AM 1.5 G filter and calibrated by a standard Si reference cell. Solar cell *J–V* curves were scanned in the reverse (from 1.3 to 0 V) and forward (from 0 to 1.3 V) directions with a fixed voltage interval of 10 mV and dwelling time of 100 ms by setting the delay at each voltage step before measuring the current. The device size was 0.04 cm^2 and a mask with an area of 0.03 cm^2 was used in the solar cell *J–V* measurements. For V_{oc} versus light intensity characterization, the light intensity was adjusted by placing an optical wheel filter in front of the incident solar beam and calibrated using a certified Si reference cell. EQE spectra were measured by a Newport external quantum measurement system (Model 66920). Dark current transport and electron-only devices were characterized by the same setup for solar cell testing in dark condition and the *J–V* curves were fitted by using Original Pro 2015 data analysis software with customized codes. AFM topographic images were captured by using a Bruker multimode 8 microscope system in the tapping mode. XRD patterns were recorded by using a Rigaku D/MAX-TTRIII3 (CBO) X-ray diffractometer equipped with a push-plug gobel mirror and a monochromatic CuKα (λ = 1.5405 Å) radiation source. GIWAXS measurements were obtained on a Xenocs Xeuss SAXS/WAXS beamline system based on an X-ray wavelength of 0.6887 Å. The reflection and transmittance spectroscopy were obtained by using a UV–vis spectrometer (PerkinElmer Lambda 650/850/950 UV–vis spectrophotometer) in the spectral range of 200–850 nm. PL decay kinetics were measured by a HORIBA Jobin-Yvon Fluorolog-III fluorimeter in the transient mode with the excitation provided by a 509 nm semiconductor diode laser with the data analyzed by the Data Analysis Software. TPC and TPV were measured by applying a 488 nm solid state laser (Coherent OBIS CORE 488LS) with a pulse width of ≈30 ns. The current traces were recorded by a mixed domain oscilloscope (Tektronix MDO3032) through converting the registered voltage drop across a 2 Ω resistor load connected in series to the solar cell. TPV measurements were performed on the solar cell at open-circuit condition with the same pulsed laser. The photovoltage traces were registered by the oscilloscope with an external 10 MΩ resistor in series. Femtosecond pump-probe TA measurements were performed at power density of 2.57 μJ cm^{-2}. The femtosecond laser pulse was generated by a Ti:sapphire femtosecond regenerative amplifier with 1030 nm wavelength and 100 kHz repetition rate (Coherence) and served as both pump and probe beams. The pump pulse with a wavelength of 500 nm and duration of 50 fs generated via a second harmonic generator (SHG) was used to excite all the samples and the probe beam was detected by a high-speed spectrometer (HELIOS, Ultrafast Systems). The wavelength range of the detector was set from 500 to 850 nm, and the spot diameter of TA is ≈1030 nm as evaluated by imaging the laser spot. All experiments were carried out at room temperature (i.e., T = 300 K).

Supporting Information

Supporting Information is available from the Wiley Online Library or from the author.

Acknowledgements

This work was financially supported by the National Natural Science Foundation of China (NSFC) with grant No. 21875012, 21674006, and 21773045. H.Z. thanks the National Key Research and Development Program of China (2017YFA0206600), and the Chinese Academy of Sciences (100 Top Young Scientists Program). Y.Z. thanks the "111 Project" (B14009). The work was also supported by the Academic Excellence Foundation of BUAA for PhD Students.

Conflict of Interest

The authors declare no conflict of interest.

Keywords

2D RP phase perovskites, crystal orientation, multi-phase alignments, quantum well effect, slow post-annealing

Received: June 19, 2019
Revised: August 19, 2019
Published online: September 2, 2019

[1] H.-S. Kim, C.-R. Lee, J.-H. Im, K.-B. Lee, T. Moehl, A. Marchioro, S.-J. Moon, R. Humphry-Baker, J.-H. Yum, J. E. Moser, M. Graetzel, N.-G. Park, *Sci. Rep.* **2012**, *2*, 591.
[2] J. Burschka, N. Pellet, S.-J. Moon, R. Humphry-Baker, P. Gao, M. K. Nazeeruddin, M. Graetzel, *Nature* **2013**, *499*, 316.
[3] X. Zhang, S. Bi, J. Zhou, S. You, H. Zhou, Y. Zhang, Z. Tang, *J. Mater. Chem. C* **2017**, *5*, 9376.
[4] F. Zhang, D. H. Kim, H. Lu, J. S. Park, B. W. Larson, J. Hu, L. Gao, C. Xiao, O. G. Reid, X. Chen, Q. Zhao, P. F. Ndione, J. J. Berry, W. You, A. Walsh, M. C. Beard, K. Zhu, *J Am. Chem. Soc.* **2019**, *141*, 5972.
[5] Y. Deng, X. Zheng, Y. Bai, Q. Wang, J. Zhao, J. Huang, *Nat. Energy* **2018**, *3*, 560.
[6] W. S. Yang, B.-W. Park, E. H. Jung, N. J. Jeon, Y. C. Kim, D. U. Lee, S. S. Shin, J. Seo, E. K. Kim, J. H. Noh, S. I. Seok, *Science* **2017**, *356*, 1376.
[7] Z. Wu, R. Raga Sonia, J. Juarez-Perez Emilio, X. Yao, Y. Jiang, K. Ono Luis, Z. Ning, H. Tian, Y. Qi, *Adv. Mater.* **2017**, *30*, 1703670.
[8] X. Zhang, X. Ren, B. Liu, R. Munir, X. Zhu, D. Yang, J. Li, Y. Liu, D.-M. Smilgies, R. Li, Z. Yang, T. Niu, X. Wang, A. Amassian, K. Zhao, S. Liu, *Energy & Environ. Sci.* **2017**, *10*, 2095.
[9] Y. Chen, Y. Sun, J. Peng, J. Tang, K. Zheng, Z. Liang, *Adv. Mater.* **2018**, *30*, 1703487.
[10] H. Tsai, W. Nie, J. Blancon, C. C. Stoumpos, R. Asadpour, B. Harutyunyan, A. J. Neukirch, R. Verduzco, J. J. Crochet, S. Tretiak, L. Pedesseau, J. Even, M. A. Alam, G. Gupta, J. Lou, P. M. Ajayan, M. J. Bedzyk, M. G. Kanatzidis, A. D. Mohite, *Nature* **2016**, *536*, 312.
[11] L. Mao, C. C. Stoumpos, M. G. Kanatzidis, A. D. Mohite, *J. Am. Chem. Soc.* **2019**, *141*, 1171.
[12] X. Xiao, J. Dai, Y. Fang, J. Zhao, X. Zheng, S. Tang, P. N. Rudd, X. C. Zeng, J. Huang, *ACS Energy Lett.* **2018**, *3*, 684.
[13] D. H. Cao, C. C. Stoumpos, O. K. Farha, J. T. Hupp, M. G. Kanatzidis, *J. Am. Chem. Soc.* **2015**, *137*, 7843.
[14] C. Liang, D. Zhao, Y. Li, X. Li, S. Peng, G. Shao, G. Xing, *Energy Environ. Mater.* **2018**, *1*, 221.
[15] M. Safdari, D. Phuyal, B. Philippe, P. H. Svensson, S. M. Butorin, K. O. Kvashnina, H. Rensmo, L. Kloo, J. M. Gardner, *J. Mater. Chem. A* **2017**, *5*, 11730.

[16] T. M. Koh, J. Huang, I. Neogi, P. P. Boix, S. G. Mhaisalkar, N. Mathews, *ACS Appl. Mater. Interfaces* **2017**, *9*, 28743.
[17] C. Ma, C. Leng, Y. Ji, X. Wei, K. Sun, L. Tang, J. Yang, W. Luo, C. Li, Y. Deng, S. Feng, J. Shen, S. Lu, C. Du, H. Shi, *Nanoscale* **2016**, *8*, 18309.
[18] Y. Chen, Y. Sun, J. Peng, W. Zhang, X. Su, K. Zheng, T. Pullerits, Z. Liang, *Adv. Energy Mater.* **2017**, *7*, 1700162.
[19] G. Wu, J. Zhou, J. Zhang, R. Meng, B. Wang, B. Xue, X. Leng, D. Zhang, X. Zhang, S. Bi, Q. Zhou, Z. Wei, H. Zhou, Y. Zhang, *Nano Energy* **2019**, *58*, 706.
[20] C. M. M. Soe, W. Nie, C. C. Stoumpos, H. Tsai, J.-C. Blancon, F. Liu, J. Even, T. J. Marks, A. D. Mohite, M. G. Kanatzidis, *Adv. Energy Mater.* **2018**, *8*, 1700979.
[21] W. Ke, L. Mao, C. C. Stoumpos, J. Hoffman, I. Spanopoulos, A. D. Mohite, M. G. Kanatzidis, *Adv. Energy Mater.* **2019**, *9*, 1803384.
[22] L. Gao, F. Zhang, C. Xiao, X. Chen, B. W. Larson, J. J. Berry, K. Zhu, *Adv. Funct. Mater.* **2019**, 1901652.
[23] X. Zhang, G. Wu, W. Fu, M. Qin, W. Yang, J. Yan, Z. Zhang, X. Lu, H. Chen, *Adv. Energy Mater.* **2018**, *8*, 1702498.
[24] H. Tsai, R. Asadpour, J. C. Blancon, C. C. Stoumpos, J. Even, P. M. Ajayan, M. G. Kanatzidis, M. A. Alam, A. D. Mohite, W. Nie, *Nat Commun.* **2018**, *9*, 2130.
[25] Y. Liao, H. Liu, W. Zhou, D. Yang, Y. Shang, Z. Shi, B. Li, X. Jiang, L. Zhang, L. N. Quan, R. Quintero-Bermudez, B. R. Sutherland, Q. Mi, E. H. Sargent, Z. Ning, *J. Am. Chem. Soc.* **2017**, *139*, 6693.
[26] X. Zhang, R. Munir, Z. Xu, Y. Liu, H. Tsai, W. Nie, J. Li, T. Niu, D. M. Smilgies, M. G. Kanatzidis, A. D. Mohite, K. Zhao, A. Amassian, S. F. Liu, *Adv. Mater.* **2018**, *30*, 1707166.
[27] C. Liang, D. Zhao, Y. Li, X. Li, S. Peng, G. Shao, G. Xing*Energy Environ. Mater.* **2018**, *1*, 221.
[28] Y. Lin, Y. Fang, J. Zhao, Y. Shao, S. J. Stuard, M. M. Nahid, H. Ade, Q. Wang, J. E. Shield, N. Zhou, A. M. Moran, J. Huang, *Nat. Commun.* **2019**, *10*, 1008.
[29] J. Liu, J. Leng, K. Wu, J. Zhang, S. Jin, *J. Chem. Soc.* **2017**, *139*, 1432.
[30] Y. Fu, W. Zheng, X. Wang, M. P. Hautzinger, D. Pan, L. Dang, J. C. Wright, A. Pan, S. Jin, *J. Am. Chem. Soc.* **2018**, *140*, 15675.
[31] S. Bi, X. Zhang, L. Qin, R. Wang, J. Zhou, X. Leng, X. Qiu, Y. Zhang, H. Zhou, Z. Tang, *Chem. - Eur. J.* **2017**, *23*, 14650.
[32] H. Yu, H. Lu, F. Xie, S. Zhou, N. Zhao, *Adv. Funct. Mater.* **2016**, *26*, 1411.
[33] P. Calado, A. M. Telford, D. Bryant, X. Li, J. Nelson, B. C. O'Regan, P. R. F. Barnes, *Nat. Commun.* **2016**, *7*, 13831.
[34] Z. Li, C. Xiao, Y. Yang, S. P. Harvey, D. H. Kim, J. A. Christians, M. Yang, P. Schulz, S. U. Nanayakkara, C.-S. Jiang, J. M. Luther, J. J. Berry, M. C. Beard, M. M. Al-Jassim, K. Zhu, *Energy Environ. Sci.* **2017**, *10*, 1234.
[35] Y. Xing, C. Sun, H. L. Yip, G. C. Bazan, F. Huang, Y. Cao, *Nano Energy* **2016**, *26*, 7.
[36] J. Peng, Y. Wu, W. Ye, D. A. Jacobs, H. Shen, X. Fu, Y. Wan, T. Duong, N. Wu, C. Barugkin, H. T. Nguyen, D. Zhong, J. Li, T. Lu, Y. Liu, M. N. Lockrey, K. J. Weber, K. R. Catchpole, T. P. White, *Energy Environ. Sci.* **2017**, *10*, 1792.
[37] Y. Liang, H. Wang, L. Liu, P. Wu, W. Cui, J. G. McEvoy, Z. Zhang, *J. Mater. Sci.* **2015**, *50*, 6935.
[38] X. Zhu, J. Lee, W. D. Lu, *Adv. Mater.* **2017**, *29*, 1700527.
[39] D. Baran, T. Kirchartz, S. Wheeler, S. Dimitrov, M. Abdelsamie, J. Gorman, R. S. Ashraf, S. Holliday, A. Wadsworth, N. Gasparini, P. Kaienburg, H. Yan, A. Amassian, C. J. Brabec, J. R. Durrant, I. McCulloch, *Energy Environ. Sci.* **2016**, *9*, 3783.
[40] X. Liu, B. Xie, C. Duan, Z. Wang, B. Fan, K. Zhang, B. Lin, F. J. M. Colberts, W. Ma, R. A. J. Janssen, F. Huang, Y. Cao, *J, Mater, Chem, A* **2018**, *6*, 395.
[41] Q. Xue, Y. Bai, M. Liu, R. Xia, Z. Hu, Z. Chen, X.-F. Jiang, F. Huang, S. Yang, Y. Matsuo, H.-L. Yip, Y. Cao, *Adv. Energy Mater.* **2017**, *7*, 1602333.
[42] M. I. Saidaminov, V. Adinolfi, R. Comin, A. L. Abdelhady, W. Peng, I. Dursun, M. Yuan, S. Hoogland, E. H. Sargent, O. M. Bakr, *Nat. Commun.* **2015**, *6*, 8724.
[43] G. Wu, J. Zhou, R. Meng, B. Xue, H. Zhou, Z. Tang, Y. Zhang, *Phys. Chem. Chem. Phys.* **2019**, *21*, 3106.
[44] K. Tvingstedt, L. Gil-Escrig, C. Momblona, P. Rieder, D. Kiermasch, M. Sessolo, A. Baumann, H. J. Bolink, V. Dyakonov, *ACS Energy Lett.* **2017**, *2*, 424.
[45] M. I. Saidaminov, A. L. Abdelhady, B. Murali, E. Alarousu, V. M. Burlakov, W. Peng, I. Dursun, L. Wang, Y. He, G. Maculan, A. Goriely, T. Wu, O. F. Mohammed, O. M. Bakr, *Nat. Commun.* **2015**, *6*, 7586.
[46] D. Liu, C. Yang, R. R. Lunt, *Joule* **2018**, *2*, 1827.
[47] K. Liu, S. Chen, J. Wu, H. Zhang, M. Qin, X. Lu, Y. Tu, Q. Meng, X. Zhan, *Energy Environ. Sci.* **2018**, *11*, 3463.
[48] D. Perez-Del-Rey, D. Forgacs, E. M. Hutter, T. J. Savenije, D. Nordlund, P. Schulz, J. J. Berry, M. Sessolo, H. J. Bolink, *Adv. Mater.* **2016**, *28*, 9839.
[49] S. Ahmad, P. Fu, S. Yu, Q. Yang, X. Liu, X. Wang, X. Wang, X. Guo, C. Li, *Joule* **2019**, *3*, 794.
[50] Z. Zhou, S. Pang, Z. Liu, H. Xu, G. Cui, *J. Mater. Chem. A* **2015**, *3*, 19205.
[51] Y. Zhang, P. Wang, M.-C. Tang, D. Barrit, W. Ke, J. Liu, T. Luo, Y. Liu, T. Niu, D.-M. Smilgies, Z. Yang, Z. Liu, S. Jin, M. G. Kanatzidis, A. Amassian, S. F. Liu, K. Zhao, *J. Am. Chem. Soc.* **2019**, *141*, 2684.
[52] N. Wang, Y. Zhou, M.-G. Ju, H. F. Garces, T. Ding, S. Pang, X. C. Zeng, N. P. Padture, X. W. Sun, *Adv. Energy Mater.* **2016**, *6*, 1601130.
[53] Z. Wang, Q. Lin, F. P. Chmiel, N. Sakai, L. M. Herz, H. J. Snaith, *Nat. Energy* **2017**, *2*, 17135.
[54] T. Zhang, M. I. Dar, G. Li, F. Xu, N. Guo, M. Grätzel, Y. Zhao, *Sci. Adv.* **2017**, *3*, 1700841.
[55] D. Liu, Q. Wang, C. J. Traverse, C. Yang, M. Young, P. S. Kuttipillai, S. Y. Lunt, T. W. Hamann, R. R. Lunt, *ACS Nano* **2018**, *12*, 876.
[56] X. Liu, Z. Liu, H. Ye, Y. Tu, B. Sun, X. Tan, T. Shi, Z. Tang, G. Liao, *Electrochim. Acta* **2018**, *288*, 115.